

# **SARS-CoV-2 direct cardiac damage through spike-mediated cardiomyocyte fusion**

Jay W. Schneider<sup>1\*</sup>, David R. Pease<sup>1‡</sup>, Chanakha K. Navaratnarajah<sup>2‡</sup>, Peter Halfmann<sup>3</sup>, Daniel J. Clemens<sup>4</sup>, Dan Ye<sup>4,5</sup>, Chang Sung Kim<sup>4,5</sup>, Alison Barkhymer<sup>2</sup>, Stephen Cohle<sup>6</sup>, Aron Banks<sup>7</sup>, Arpit Mehta<sup>7</sup>, Joseph Rantus<sup>7</sup>, Tim L. Emmerzaal<sup>8</sup>, Tamás Kozicz<sup>8</sup>, Kyle G. Howell<sup>9</sup>, Jon E. Charlesworth<sup>9</sup>, Trace A. Christensen<sup>9</sup>, Yoshihiro Kawaoka<sup>3,10</sup>, Leslie T. Cooper<sup>11</sup>, Michael J. Ackerman<sup>4,5</sup>, Roberto Cattaneo<sup>2</sup> & Wanek Family Program for HLHS-Stem Cell Pipeline

<sup>1</sup>Discovery Engine/Program for Hypoplastic Left Heart Syndrome, Mayo Clinic, Rochester, Minnesota 55905, USA

<sup>2</sup>Department of Molecular Medicine, Mayo Clinic, Rochester, Minnesota 55905, USA

<sup>3</sup>Influenza Research Institute, Department of Pathobiological Sciences, School of Veterinary Medicine, University of Wisconsin-Madison, Madison, Wisconsin 53711, USA

<sup>4</sup>Department of Molecular Pharmacology & Experimental Therapeutics, Windland Smith Rice Sudden Death Genomics Laboratory, Mayo Clinic Graduate School of Biomedical Sciences, Rochester, Minnesota 55905, USA

<sup>5</sup>Departments of Cardiovascular Medicine and Pediatric and Adolescent Medicine, Divisions of Heart Rhythm Services and Pediatric Cardiology, Mayo Clinic, Rochester, Minnesota 55905, USA

<sup>6</sup>Spectrum Health, Blodgett Hospital Pathology, Grand Rapids, Michigan 49506, USA

<sup>7</sup>CardioPath LLC, Doral, Florida 33172, USA

<sup>8</sup>Departments of Biochemistry and Molecular Biology and Clinical Genomics, Mayo Clinic, Rochester, Minnesota 55905

<sup>9</sup>Mayo Microscopy and Cell Analysis Core, Mayo Clinic, Rochester, Minnesota 55905, USA

<sup>10</sup>Division of Virology, Department of Microbiology and Immunology, Institute of Medical Science, University of Tokyo, 108-8639 Tokyo, Japan

<sup>11</sup>Department of Cardiovascular Medicine, Mayo Clinic, Jacksonville, Florida 32224, USA

<sup>‡</sup> Authors contributed equally.

\* To whom correspondence should be addressed.

## Summary

Viruses spread between hosts through particles, but within hosts, viral genomes can spread from cell to cell through fusion, evading antiviral defenses and obviating costly infectious virion production<sup>1-3</sup>. Billions of electromechanically coupled cardiomyocytes (CMs) make myocardium inherently vulnerable to pathological electromechanical short circuits caused by intercellular viral spread<sup>4-6</sup>. Beyond respiratory illness, COVID-19 affects the heart<sup>7</sup> and cardiac injury and arrhythmias are serious public health concerns<sup>8-12</sup>. By studying myocardium of a young woman who died suddenly, diagnosed postmortem with COVID-19, we discovered highly focal myocardial SARS-CoV-2 infection spreading from one CM to another through intercellular junctions identified by highly concentrated sarcolemmal t-tubule viral spike glycoprotein. SARS-CoV-2 permissively infected beating human induced pluripotent stem cell (hiPSC)-CMs building multinucleated cardiomyotubes (CMTs) through cell type-specific fusion driven by proteolytically-activated spike glycoprotein. Recombinant spike glycoprotein, co-localizing to sarcolemma and sarcoplasmic reticulum, produced multinucleated CMTs with pathological structure, electrophysiology and  $\text{Ca}^{2+}$  excitation-contraction coupling. Blocking cleavage, a peptide-based protease inhibitor neutralized SARS-CoV-2 spike glycoprotein pathogenicity. We conclude that SARS-CoV-2 spike glycoprotein, efficiently primed, activated and strategically poised during biosynthesis, can exploit the CM's inherent membranous connectivity to drive heart damage directly, uncoupling clinically common myocardial injury from lymphocytic myocarditis, often suspected but rarely confirmed in COVID-19.

## Sudden cardiac death in COVID-19

A 35 year-old Hispanic woman, 3 months post-partum, had one week of mild fever and cough, felt lightheaded, went to rest and was later found dead by her husband. At autopsy, the medical examiner diagnosed fulminant lymphocytic myocarditis and, although postmortem COVID-19 testing (nasal swab RT-PCR and serum anti-spike glycoprotein IgG) was positive, pathognomonic bronchopulmonary COVID-19 pathology was lacking. To clarify the cause of death, we obtained myocardium for molecular and immunohistopathological analysis. Immunofluorescence (IF) confocal microscopy identified clusters of SARS-CoV-2 spike glycoprotein-(+) CMs with intense staining localized to linearly-arrayed t-tubules, concentrated at the lateral margins between adjacent cells (Fig. 1a, area circled in yellow). The spike glycoprotein signal alone is presented in (Fig. 1b) and linearly arrayed t-tubules are highlighted by white arrows. While two spike glycoprotein-(+) infiltrating inflammatory cells are also present in (Fig. 1a, white arrows), these are more clearly evident by IF confocal microscopy for the SARS-CoV-2 nucleocapsid protein shown in (Ext. Data Fig. 1). Spike glycoprotein highly concentrated in t-tubule networks of adjacent CMs suggested the possibility of cell-to-cell conduits<sup>3</sup>. If viral spike, a membrane fusion protein, opens pores between CMs, these newly created cell-cell conduits, even if microscopic, could be precarious, functionally short circuiting electrically excitable myocardium. We formulated the following hypothesis to explain this patient's sudden cardiac death: SARS-CoV-2, brought to the myocardium via infected immune cells, spread from one CM to another through spike glycoprotein generated conduits. Intercellular connections created by spike glycoprotein drove membrane fusion that provided the pathoanatomical substrate for aberrant electrophysiological activity, electromechanical dysfunction and fatal arrhythmia.

## Cardiomyocyte infection by SARS-CoV-2

To explore this hypothesis *in vitro*, we infected hiPSC-CMs at day-20 of cardiac differentiation with SARS-CoV-2. We showed by gene expression microarray in H9 human embryonic stem cells (hESCs) that transcript levels of the SARS-CoV-2 receptor, ACE2, peaked at day-20 of the cardiac differentiation program (Ext. Data Fig. 2). Super resolution immunofluorescence confocal microscopy confirmed high level ACE2 expression in day-20 hiPSC-CMs positively identified by striated F-actin organization (Fig. 2a). Cardiomyocyte ACE2 receptors clustered in raft-like puncta diffusely distributed across the sarcolemma and, germane to our hypothesis, extended into filopodia contacting adjacent CMs (Fig. 2a, arrow highlights filopodia). Notably, mRNA encoding the ACE2-associated membrane protease, TMPRSS2, which mediates S1/S2 spike glycoprotein cleavage in the lung thereby enabling viral entry during pulmonary infection, was not detected by microarray in hESC-CMs at any timepoint (Ext. Data Fig. 2).

SARS-CoV-2, even at low multiplicity of 0.01, permissively infected spontaneously beating CMs (Fig. 2b). Transmission electron microscopy (TEM) analyses revealed canonical double-membrane vesicles, endoplasmic reticulum-Golgi intermediate complex and smooth-walled exocytic vesicles containing numerous 65-90 nm particles

(pseudo-colored cyan) identified as progeny virions with characteristic helical ribonucleocapsids surrounded by a membrane (Fig. **2b** and Ext. Data Fig. **3**).

Scanning EM (SEM) (Fig. **2c**) of an hiPSC-CM at a later stage of the viral replication cycle demonstrated saturation of the CM surface with SARS-CoV-2 virus particles showing knob-like spikes (Fig. **2c**, upper right inset box) distributed in a uniform monolayer and extending onto pseudo and filopodia capable of directly contacting neighboring CMs (Fig. **2c**, lower right inset box).

We measured hiPSC-CM SARS-CoV-2 virus production by plaque forming unit (PFU) assay on Vero cells (Fig. **2d**). Plaque counts, shown by crystal violet staining of virus-infected Vero monolayers (right panels), demonstrated striking productivity for a functionally differentiated (non-cancer) cell type. Immunoblot analyses of viral spike glycoprotein (S), nucleocapsid (N) and membrane (M) proteins confirmed high expression levels and accurate protein processing (Ext. Data Fig. **4**). Likewise, immunocytochemistry of infected hiPSC-CMs confirmed expression of all three viral proteins localized to the expected subcellular compartments (Ext. Data Fig. **4**; note that immature hiPSC-CMs lack t-tubules). Taken together, these analyses confirmed highly productive infection of hiPSC-CMs by SARS-CoV-2.

SARS-CoV-2 infected hiPSC-CMs produced multinucleated giant cells, called cardiomyotubes (CMTs), already evident at 24 hours post-infection, the earliest time point examined (Fig. **3a** and Ext. Data Fig. **5**). M-protein positive SARS-CoV-2 infected hiPSC-CMs demonstrated sarcomeric disassembly/fragmentation shown by disintegration of  $\alpha$ -actinin Z-discs into randomly distributed puncta (insets of Figs. **3a** and **3b**).

To quantify SARS-CoV-2 mediated hiPSC-CM fusion,  $\alpha$ -actinin and SARS-CoV-2 M protein co-labeled cells were imaged by IF confocal microscopy and CMTs were counted. While no CMTs were observed for mock infected cells, ~4 CMTs were counted per field of SARS-CoV-2 infected cells (Fig. **3e**, CMT index). As an alternative method to quantify fusion, we counted the number of nuclei per cell, finding an average of about 2 in infected cells, double that counted in the mock control (Fig. **3e**, nuclearity index).

Fig. **3c** shows an hiPSC-CM heavily carpeted with SARS-CoV-2 particles (rightmost cell) fused with two much less heavily carpeted hiPSC-CMs at upper and lower left with boundaries clearly demarcated, creating a patchwork mosaic. The inset magnifies the fusion boundary between hiPSC-CMs highlighted by the white box.

Human iPSC-CMs, like their postnatal pig CM counterparts (Schneider et al., *Nature Medicine*, Dysregulated ribonucleoprotein granules promote cardiomyopathy in *RBM20* gene-edited pigs, DOI: 10.1038/s41591-020-1087-x, 2020) (Ext. Data Fig. **5b**) can produce multinucleated CMTs by endo cell cycle. We assessed endo cell cycle's role here by pulse labeling of asynchronously growing hiPSC-CMs using the DNA synthesis marker EdU (Fig. **3d**): if produced by endomitosis, all sibling nuclei within an individual CMT would be synchronized, equivalently (dilutionally) labeled by EdU. In contrast, Fig. **3d** shows a mixture of unsynchronized, differentially labeled nuclei in the CMT. This can only be the result of viral-mediated hiPSC-CM fusion.

## **Spike protein-induced cardiomyotubes**

To characterize the mechanism of SARS-CoV-2 spike glycoprotein-induced fusion, we engineered a full-length recombinant spike glycoprotein molecule fused to modified Emerald green fluorescent protein (mEm) at its C-terminus (CoV-2 S-mEm) (Fig. 4a). We validated this reagent in Vero cells that, like hiPSC-CMs, are ACE2-(+) but TMPRSS2(-). In these cells, recombinant CoV-2 S-mEm was cleaved appropriately at the S1/S2 furin cleavage site (Ext. Data Fig. 6a). Super resolution confocal microscopy localized this spike protein to hair-like plasma membrane extensions (Ext. Data Fig. 6b). Fluorescent activated cell sorting confirmed spike protein cell surface expression (Ext. Data Fig. 6c). Live cell imaging tracked spread of signal from cell to cell through membrane fusion, generating giant syncytia (Ext. Data Fig. 6d and Supplemental Video 1).

We next evaluated SARS-CoV-2 spike glycoprotein fusion in hiPSC-CMs. Super resolution confocal microscopy of hiPSC-CMs transfected with recombinant CoV-2 S-mEm demonstrated fluorescent signal at the tips of dynamic pseudo- and filopodia contacting neighboring hiPSC-CMs (Fig. 4b, circle). Despite overall transfection efficiency <5%, recombinant CoV-2 S-mEm expressing hiPSC-CMs produced giant CMTs, recognizable within 6 hours of transfection (Fig. 4c and Supplemental Video 1). EdU pulse-labelling demonstrated cell cycle asynchrony confirming fusion rather than endomitosis (Fig. 4d).

Like their infected counterparts, giant multinucleated CMTs produced by CoV-2 spike protein-driven fusion were characterized by structural derangements that included circular or oval enucleated cytoskeletal “corpses” shown by F-actin phalloidin staining (Fig. 4e, white arrows). Nuclei in CMTs frequently arranged themselves in clusters or rosettes (Fig. 4f), although we occasionally observed more-physiological linear rows of nuclei (Ext. Data Fig. 5a), reminiscent of pig CMT produced by endomitosis (Ext. Data Fig. 5b).

## **Calcium tsunamis in cardiomyotubes**

We then characterized the electrophysiology of CMTs fused by recombinant CoV-2 S-mEm glycoprotein through sarcolemma patch clamping (Fig. 5a). Fig. 5b shows action potential tracings evoked in control hiPSC-CMs or recombinant CoV-2 S-mEm multinucleated CMTs. CMTs demonstrated markedly prolonged action potential duration (APD) with an average APD90 of 590 versus 420 ms in control hiPSC-CMs (Ext. Data Fig. 7a), shown graphically for APD50 and APD90 in (Ext. Data Fig. 7b and 7c), respectively.

CMTs demonstrated markedly elevated membrane capacitance compared to control hiPSC-CMs (Fig. 5c) and displayed dysrhythmias notable for delayed afterdepolarizations (DADs) and erratic beating frequency (Fig. 5d, tracing in red, DAD denoted by black arrow). Compared to CMTs, control hiPSC-CMs never exhibited DADs (Fig. 5e). Additional examples of pathological spontaneous rhythms recorded from CMTs are shown in (Ext. Data Fig. 7d) with DADs highlighted by arrows.

We studied  $\text{Ca}^{2+}$  handling in recombinant SARS-CoV-2 spike protein produced CMTs and observed markedly pathological  $\text{Ca}^{2+}$  flux, sparks and tsunami-like waves shown by imaging and corresponding tracings (Fig. 5f, Ext. Data Fig. 8a-c), but best appreciated by video microscopy (Supplemental Videos 3-5). Abnormal  $\text{Ca}^{2+}$  flux in CoV-2 S transfected multinucleated CMTs correlated with colocalization of spike glycoprotein to the sarcoplasmic reticulum (Fig. 5g).

We then sought to interfere with this process using Decanoyl-RVKR-CMK, a cell-permeable, peptide-based molecule that irreversibly blocks the catalytic site of furin, a ubiquitous protease located in the Golgi. This compound attenuated cell fusion (Fig. 5h) as well as the tsunami (Fig. 5i) and spark (Ext. Data Fig. 8d)  $\text{Ca}^{2+}$  imaging phenotype, correlating with a drastically reduced number of CMTs in SARS-CoV-2 S glycoprotein transfected hiPSC-CMs (Fig. 5h). The analogous experiment in Vero cells confirmed biochemical suppression of S1/S2 cleavage and fusion blockade by Decanoyl-RVKR-CMK (Ext. Data Fig. 8e).

## Discussion

We show here that the SARS-CoV-2 spike glycoprotein is a powerful fusogen of ACE2 receptor-(+) hiPSC-CMs. We link CMT generation by cell fusion to electrical dysfunction in fatal cardiac injury associated with COVID-19. While cell-cell fusion is not immediately evident in our patient's autopsy tissue, fusion pores may open, creating cell-cell conduits that do not extend because of cytoskeletal constraints, as characterized for other viral infections in vivo<sup>13</sup>. We suggest that SARS-CoV-2 spike glycoprotein-induced membrane changes directly injure CMs, heightening cardiac arrhythmia risk even at low viral load and in the absence of widespread lymphocytic myocarditis-mediated tissue destruction. This result explains the mismatch between cardiac injury, frequently observed in COVID-19<sup>14</sup>, and lymphocytic myocarditis, which is extremely rare, an until now unsolved clinical paradox<sup>5,6,15</sup>.

Cardiac damage in COVID-19 acute respiratory distress syndrome, multisystem inflammatory syndrome and shock is also caused by microthrombosis and cardiotoxic catecholamine or inflammatory-cytokine storms<sup>16-19</sup>, but these severe conditions are uncommon. Beyond SARS-CoV-2<sup>9,12,14,20-23</sup>, its predecessors SARS-CoV<sup>24</sup> and Middle East respiratory syndrome (MERS)<sup>25</sup> cause cardiac injury. Moreover, Rabbit coronavirus (RbCV), discovered more than three decades ago, produces sufficient cardiac injury to cause cardiomyopathy<sup>26-28</sup>, and finally, myocardial viral nucleic acids are frequently observed in primate<sup>29</sup> and murine<sup>30</sup> SARS-CoV-2 infection models, but notably again without lymphocytic myocarditis.

Human iPSC-CMs may have immature innate immune defenses and thus be more permissive to SARS-CoV-2 infection. Nevertheless, virus-induced pathological modification of plasma membranes occurs even in the absence of complete viral replication<sup>31,32</sup>. In particular, expression of spike glycoprotein alone in hiPSC-CMs induced  $\text{Ca}^{2+}$  sparks, tsunami-like  $\text{Ca}^{2+}$  waves and electromechanical abnormalities. Expression of proteolytically primed and activated spike glycoprotein at the CM surface might contribute, through cell-cell fusion, to the natural history of cardiomyopathy evolving decades after successful clearance of virus<sup>4,8,33</sup>.

Sequential spike glycoprotein cleavage at two sites governs SARS-CoV-2 cell entry and pathogenesis<sup>34</sup>. While cleavage by TMPRSS2 is critical for entry into lung epithelial cells<sup>34</sup>, CMs do not express this protease. SARS-CoV-2 spike protein cleavage at S1/S2 site by furin contributes to cardiac pathogenicity: in hiPSC-CMs efficient spike protein proteolytic processing and CMTs formation are blocked by a furin inhibitor.

We analyzed the function of the spike proteins of other coronaviruses in hiPSC-CMs: while the MERS coronavirus spike glycoprotein drove CMT production with slower kinetics (Ext. Data Fig. **9**), the spike glycoproteins of SARS-CoV and of the common cold coronavirus HCoV-229E were inactive, mirroring results in Vero cells (data not shown). The protease driving S2' cleavage of the SARS-CoV-2 spike glycoprotein in CMs and Vero cells remains to be identified.

Taken together, these results demonstrate that SARS-CoV-2 spike glycoprotein, autonomously spreading from CM to CM, can directly produce cellular damage and dysfunction that may explain the cardiac injury frequently observed clinically in COVID-19 despite low myocardial viral load and absence of classic lymphocytic myocarditis or cytopathic tissue destruction.

- 1 Sattentau, Q. Avoiding the void: cell-to-cell spread of human viruses. *Nat Rev Microbiol* **6**, 815-826, doi:10.1038/nrmicro1972 (2008).
- 2 Sewald, X., Motamedi, N. & Mothes, W. Viruses exploit the tissue physiology of the host to spread in vivo. *Curr Opin Cell Biol* **41**, 81-90, doi:10.1016/j.ceb.2016.04.008 (2016).
- 3 Cifuentes-Munoz, N., Dutch, R. E. & Cattaneo, R. Direct cell-to-cell transmission of respiratory viruses: The fast lanes. *PLoS Pathog* **14**, e1007015, doi:10.1371/journal.ppat.1007015 (2018).
- 4 Cooper, L. T., Jr. Myocarditis. *N Engl J Med* **360**, 1526-1538, doi:10.1056/NEJMr0800028 (2009).
- 5 Mitrani, R. D., Dabas, N. & Goldberger, J. J. COVID-19 cardiac injury: Implications for long-term surveillance and outcomes in survivors. *Heart Rhythm*, doi:10.1016/j.hrthm.2020.06.026 (2020).
- 6 Baldi, E. *et al.* Out-of-Hospital Cardiac Arrest during the Covid-19 Outbreak in Italy. *N Engl J Med* **383**, 496-498, doi:10.1056/NEJMc2010418 (2020).
- 7 Topol, E. J. COVID-19 can affect the heart. *Science*, doi:10.1126/science.abe2813 (2020).
- 8 Yancy, C. W. & Fonarow, G. C. Coronavirus Disease 2019 (COVID-19) and the Heart—Is Heart Failure the Next Chapter? *JAMA Cardiology*, doi:10.1001/jamacardio.2020.3575 (2020).
- 9 Zeng, J. H. *et al.* First case of COVID-19 complicated with fulminant myocarditis: a case report and insights. *Infection*, doi:10.1007/s15010-020-01424-5 (2020).
- 10 Madjid, M., Safavi-Naeini, P., Solomon, S. D. & Vardeny, O. Potential Effects of Coronaviruses on the Cardiovascular System: A Review. *JAMA Cardiol*, doi:10.1001/jamacardio.2020.1286 (2020).
- 11 Inciardi, R. M. *et al.* Cardiac Involvement in a Patient With Coronavirus Disease 2019 (COVID-19). *JAMA Cardiol*, doi:10.1001/jamacardio.2020.1096 (2020).

279 12 Irabien-Ortiz, A. *et al.* Fulminant myocarditis due to COVID-19. *Rev Esp Cardiol*  
280 *(Engl Ed)* **73**, 503-504, doi:10.1016/j.rec.2020.04.005 (2020).

281 13 Singh, B. K., Pfaller, C. K., Cattaneo, R. & Sinn, P. L. Measles Virus  
282 Ribonucleoprotein Complexes Rapidly Spread across Well-Differentiated Primary  
283 Human Airway Epithelial Cells along F-Actin Rings. *mBio* **10**,  
284 doi:10.1128/mBio.02434-19 (2019).

285 14 Puntmann, V. O. *et al.* Outcomes of Cardiovascular Magnetic Resonance  
286 Imaging in Patients Recently Recovered From Coronavirus Disease 2019  
287 (COVID-19). *JAMA Cardiology*, doi:10.1001/jamacardio.2020.3557 (2020).

288 15 Zhou, F. *et al.* Clinical course and risk factors for mortality of adult inpatients with  
289 COVID-19 in Wuhan, China: a retrospective cohort study. *Lancet* **395**, 1054-  
290 1062, doi:10.1016/S0140-6736(20)30566-3 (2020).

291 16 Zheng, Y. Y., Ma, Y. T., Zhang, J. Y. & Xie, X. COVID-19 and the cardiovascular  
292 system. *Nat Rev Cardiol*, doi:10.1038/s41569-020-0360-5 (2020).

293 17 Liu, P. P., Blet, A., Smyth, D. & Li, H. The Science Underlying COVID-19:  
294 Implications for the Cardiovascular System. *Circulation*,  
295 doi:10.1161/CIRCULATIONAHA.120.047549 (2020).

296 18 Bonow, R. O., Fonarow, G. C., O'Gara, P. T. & Yancy, C. W. Association of  
297 Coronavirus Disease 2019 (COVID-19) With Myocardial Injury and Mortality.  
298 *JAMA Cardiol*, doi:10.1001/jamacardio.2020.1105 (2020).

299 19 Hendren, N. S., Drazner, M. H., Bozkurt, B. & Cooper, L. T., Jr. Description and  
300 Proposed Management of the Acute COVID-19 Cardiovascular Syndrome.  
301 *Circulation*, doi:10.1161/CIRCULATIONAHA.120.047349 (2020).

302 20 Hu, H., Ma, F., Wei, X. & Fang, Y. Coronavirus fulminant myocarditis saved with  
303 glucocorticoid and human immunoglobulin. *Eur Heart J*,  
304 doi:10.1093/eurheartj/ehaa190 (2020).

305 21 Kim, I. C., Kim, J. Y., Kim, H. A. & Han, S. COVID-19-related myocarditis in a 21-  
306 year-old female patient. *Eur Heart J* **41**, 1859, doi:10.1093/eurheartj/ehaa288  
307 (2020).

308 22 Lindner, D. *et al.* Association of Cardiac Infection With SARS-CoV-2 in  
309 Confirmed COVID-19 Autopsy Cases. *JAMA Cardiology*,  
310 doi:10.1001/jamacardio.2020.3551 (2020).

311 23 Godfred-Cato, S. *et al.* COVID-19-Associated Multisystem Inflammatory  
312 Syndrome in Children - United States, March-July 2020. *MMWR Morb Mortal*  
313 *Wkly Rep* **69**, 1074-1080, doi:10.15585/mmwr.mm6932e2 (2020).

314 24 Oudit, G. Y. *et al.* SARS-coronavirus modulation of myocardial ACE2 expression  
315 and inflammation in patients with SARS. *Eur J Clin Invest* **39**, 618-625,  
316 doi:10.1111/j.1365-2362.2009.02153.x (2009).

317 25 Alhogbani, T. Acute myocarditis associated with novel Middle east respiratory  
318 syndrome coronavirus. *Ann Saudi Med* **36**, 78-80, doi:10.5144/0256-  
319 4947.2016.78 (2016).

320 26 Alexander, L. K., Keene, B. W., Small, J. D., Yount, B., Jr. & Baric, R. S.  
321 Electrocardiographic changes following rabbit coronavirus-induced myocarditis  
322 and dilated cardiomyopathy. *Adv Exp Med Biol* **342**, 365-370, doi:10.1007/978-1-  
323 4615-2996-5\_56 (1993).



- 27 Small, J. D. & Woods, R. D. Relatedness of rabbit coronavirus to other  
coronaviruses. *Adv Exp Med Biol* **218**, 521-527, doi:10.1007/978-1-4684-1280-  
2\_68 (1987).
- 28 Edwards, S., Small, J. D., Geratz, J. D., Alexander, L. K. & Baric, R. S. An  
experimental model for myocarditis and congestive heart failure after rabbit  
coronavirus infection. *J Infect Dis* **165**, 134-140, doi:10.1093/infdis/165.1.134  
(1992).
- 29 Munster, V. J. *et al.* Respiratory disease in rhesus macaques inoculated with  
SARS-CoV-2. *Nature* **585**, 268-272, doi:10.1038/s41586-020-2324-7 (2020).
- 30 Gu, H. *et al.* Adaptation of SARS-CoV-2 in BALB/c mice for testing vaccine  
efficacy. *Science*, doi:10.1126/science.abc4730 (2020).
- 31 Miller, S. & Krijnse-Locker, J. Modification of intracellular membrane structures  
for virus replication. *Nat Rev Microbiol* **6**, 363-374, doi:10.1038/nrmicro1890  
(2008).
- 32 Mateo, M., Generous, A., Sinn, P. L. & Cattaneo, R. Connections matter--how  
viruses use cell-cell adhesion components. *J Cell Sci* **128**, 431-439,  
doi:10.1242/jcs.159400 (2015).
- 33 Pollack, A., Kontorovich, A. R., Fuster, V. & Dec, G. W. Viral myocarditis--  
diagnosis, treatment options, and current controversies. *Nat Rev Cardiol* **12**, 670-  
680, doi:10.1038/nrcardio.2015.108 (2015).
- 34 Hoffmann, M. *et al.* SARS-CoV-2 Cell Entry Depends on ACE2 and TMPRSS2  
and Is Blocked by a Clinically Proven Protease Inhibitor. *Cell* **181**, 271-280 e278,  
doi:10.1016/j.cell.2020.02.052 (2020).

## Figure Legends

**Figure 1 | Spike glycoprotein expression by SARS-CoV-2 infected cardiomyocytes (CMs) in fatal COVID19.** **a**, IF confocal microscopy of patient myocardium showing SARS-CoV-2 spike-(+) CMs with adjacent SARS-CoV-2 spike(+) immune infiltrate (white arrows). Scale bar, 20  $\mu$ m. **b**, Isolated SARS-CoV-2 spike signal from Fig. **1a**, highlighting SARS-CoV-2 spike glycoprotein localized to linearly arrayed t-tubules (white arrows). Scale bar, 20  $\mu$ m.

**Fig 2 | Efficient SARS-CoV-2 infection of hiPSC-CMs.** **a**, IF super resolution confocal microscopy of ACE2 plasma membrane localization in fixed, non-permeabilized hiPSC-CMs. Scale bar, 10  $\mu$ m. **b**, TEM of SARS-CoV-2 infected hiPSC-CMs, 48 hours post-infection depicting SARS-CoV-2 (cyan) within vesicles. Scale bar, 400 nm. Inset panel is high magnification pseudo-colored TEM of SARS-CoV-2 viral particles, demonstrating electron-dense ribonucleocapsid structures (white arrow). Scale bar, 100 nm. **c**, SEM of SARS-CoV-2 infected hiPSC-CMs, 48 hours post-infection. Scale bar, 2  $\mu$ m. Upper inset panel is high magnification SEM showing knob-like spikes on SARS-CoV-2 viral particles. Scale bar, 100 nm. Lower inset panel is high magnification SEM of hiPSC-CM filopodia dotted with SARS-CoV-2 viral particles. Scale bar, 1  $\mu$ m. **d**, SARS-CoV-2 PFU assay from two hiPSC-CM cell lines: open squares, hiPSC-CM#1; filled dots, hiPSC-CM#2.

**Fig 3 | Cytopathic effects of SARS-CoV-2 in hiPSC-CMs.** **a**, IF confocal microscopy of SARS-CoV-2 infected hiPSC-CMs (48 hours post-infection). Scale bar, 20  $\mu$ m. **b**, IF confocal microscopy of mock infected hiPSC-CMs. Scale bar, 20  $\mu$ m. Insets show IF super resolution confocal microscopy of SARS-CoV-2 and mock infected hiPSC-CMs, respectively. Scale bars, 10  $\mu$ m. **c**, SEM of three SARS-CoV-2 infected hiPSC-CMs. Scale bar, 1  $\mu$ m. Inset shows high magnification of the surface region shown with white box. Scale bar, 500 nm. **d**, Confocal microscopy of an EdU pulse-labeled, SARS-CoV-2 infected hiPSC-CMT. Scale bar, 20  $\mu$ m. **e**, Quantification of cell fusion in SARS-CoV-2 infected and Mock infected hiPSC-CM. CMT index is the average number of CMTs per field (n=12 fields). Nuclearity index is the average number of nuclei per cell per field. (n=12 fields, two-tailed T-test).

**Fig 4 | SARS-CoV-2 spike glycoprotein induces syncytia in hiPSC-CMs.** **a**, Linear map of recombinant CoV-2 S-mEm fusion protein engineered for this study with mEmerald at the cytoplasmic tail. Cleavage at the S1/S2 furin site primes the spike protein for activation. S1, S1 subunit; S2, S2 subunit; N-/C-RBD, N-/C-terminal receptor binding domains; HR1/HR2, heptad repeat 1 and 2. The antibody 1A9, used to detect the spike protein, binds to an exposed loop located close to HR2. Decanoyl-RVKKR-CMK (Furin inhibitor I) was used to inhibit spike protein cleavage. **b**, Super resolution confocal microscopy of CoV-2 S-mEM localization to hiPSC-CM filopodia directly contacting the sarcolemma of an adjacent hiPSC-CM (yellow circle). Scale bar, 2  $\mu$ m. **c**, Live cell imaging frame of CoV-2 S-mEm transfected hiPSC-CMs demonstrating giant CMTs. Scale bar, 50  $\mu$ m. **d**, Confocal microscopy image of EdU pulse-labeled, SARS-CoV-2 S transfected hiPSC-CMT. Scale bar, 20  $\mu$ m. **e** and **f**, Confocal microscopy of SARS-CoV-2 S transfected hiPSC-CM giant CMTs. Note the enucleated actin

cytoskeletal “corpses” (e, white arrows) and the nuclei arranged in rosettes (f). Scale bars, 20  $\mu\text{m}$ .

**Fig 5 | SARS-CoV-2 spike generated electrical dysfunction rescued by furin inhibition.** **a**, Visualization of a sarcolemma patch clamp in recombinant CoV-2 S-mEm transfected hiPSC-CMT. Scale bar, 50  $\mu\text{m}$ . **b**, Action potential traces of control hiPSC-CMTs (black) and recombinant CoV-2 S-mEm transfected (red) hiPSC-CMTs paced at 1 Hz. **c**, Cell capacitance of control hiPSC-CMTs (black) and recombinant CoV-2 S-mEm transfected (red) hiPSC-CMTs. Box and whisker plot shows median, upper and lower quartile and extremes. **d**, Patch clamp traces of spontaneous beating in control hiPSC-CMTs (black) and recombinant CoV-2 S-mEm transfected (red) hiPSC-CMTs. Black arrows indicate delayed afterdepolarizations (DAD). **e**, Rate of occurrence of DADs in control hiPSC-CMTs (black) and recombinant CoV-2 S-mEm transfected (red) hiPSC-CMTs. **f**, Still frame images of Fluo-4 AM  $\text{Ca}^{2+}$  imaging in recombinant CoV-2 S transfected hiPSC-CMTs at 2 and 6 seconds after the initiation of  $\text{Ca}^{2+}$  tsunami. Yellow to red broken circles and arrow indicate direction of  $\text{Ca}^{2+}$  tsunami movement. Scale bar, 20  $\mu\text{m}$ . **g**, IF confocal microscopy of SERCA2 and S-protein co-localization in sarcoplasmic reticulum of a recombinant CoV-2 S transfected hiPSC-CMT. Scale bars, 10  $\mu\text{m}$ . **h**, Suppression of CoV-2 S induced hiPSC-CMT formation at day 5 post-transfection (red broken circles) (left panel) by 20  $\mu\text{M}$  furin inhibitor Decanoyl-RVKR-CMK (right panel) shown by crystal violet staining. Scale bar, 100  $\mu\text{m}$ . Center panel: CMT counts per field of view with box and whisker plot depicting extremes, upper and lower quartile and median. **i**, Central panel shows suppression of CoV-2 S induced  $\text{Ca}^{2+}$  tsunamis in hiPSC-CMTs (in red) paced at 1Hz by 20  $\mu\text{M}$  furin inhibitor Decanoyl-RVKR-CMK (in black, +drug) with box and whisker plot depicting extremes, upper and lower quartile and median. Left and right panels show Fluo-4 AM  $\text{Ca}^{2+}$  imaging trace examples of  $\text{Ca}^{2+}$  tsunami (red) and control (black).

## Extended Data Figure Legends

**Ext. Data Fig. 1 | Clinicopathobiological data for SARS-CoV-2 associated sudden cardiac death.** **a**, Clinical vignette of SARS-CoV-2 associated sudden cardiac death. **b**, Gross anatomical section of patient heart taken at time of autopsy (total heart weight 290 grams is normal) highlighting epicardial fat (white arrow), streak-like, patchy inflammatory infiltrate (red arrow) and normal myocardium (yellow arrow). Scale bar, 1 cm. **c**, H&E staining of patient myocardium demonstrating fulminant lymphocytic myocarditis. Black broken circle highlights cardiomyocyte necrosis and yellow broken circle highlights inflammatory infiltrate notable for eosinophils. Scale bar, 50  $\mu\text{m}$ . **d**, IHC of CD3+ (T-cell) infiltrate in patient myocardium. Scale bar, 50  $\mu\text{m}$ . **e**, IHC of CD68+ (monocyte/macrophage) infiltrate in patient myocardium. Scale bar, 50  $\mu\text{m}$ . **f**, IF confocal microscopy of patient myocardium with SARS-CoV-2 nucleocapsid-(+) inflammatory infiltrate adjacent to cardiomyocytes. MYL2 is myosin light chain-2, a cardiomyocyte-specific marker. Yellow and white arrows indicate SARS-CoV-2 nucleocapsid-(+) inflammatory cell and cardiomyocyte, respectively. Scale bar, 20  $\mu\text{m}$ .

**Ext. Data Fig. 2 | ACE2 and TMPRSS2 expression in stem cell derived**

**cardiomyocytes. a,** Gene expression Affymetrix microarray of cardiac differentiation time course in H9 human embryonic stem cells (hESCs). P (present) means transcript is significantly ( $P < 0.05$ ) and A (absent) means not significantly ( $P > 0.05$ ) expressed, comparing perfectly matched with mismatched (background) probe sets. Numerical values across an individual probe set correspond to relative transcript levels. **b,** Super resolution confocal microscopy of ACE2 in day-20 hiPSC-CMs. Scale bar, 10  $\mu\text{m}$ .

**Ext. Data Fig. 3 | Transmission electron microscopy of SARS-CoV-2 infected stem cell-derived cardiomyocytes. a,**

SARS-CoV-2 infected hiPSC-CM, 48 hours post-infection. Asterisk marks the ER-Golgi Intermediate Complex (ERGIC) containing SARS-CoV-2 viral particles and hiPSC-CM identity is confirmed by myofibrils (yellow arrows) and Z-discs (red arrows). Scale bar, 1  $\mu\text{m}$ . **b,** SARS-CoV-2 reticulovesicular network. Ribosome-studded double membrane vesicles (green arrow) and clustered membranes (yellow arrows). Scale bar, 1  $\mu\text{m}$ . **c,** SARS-CoV-2 vesicle packet (blue arrow) and mitochondria (red arrow). Scale bar, 2  $\mu\text{m}$ . **d,** SARS-CoV-2 exocytic vesicles (white arrows). Scale bar, 1  $\mu\text{m}$ .

**Ext. Data Fig. 4 | Viral protein expression in SARS-CoV-2 infected hiPSC-CMs.**

Companion immunoblots (left) and low-power IF confocal microscopy (right) of **a,** SARS-CoV-2 spike glycoprotein (S0, S2), **b,** nucleocapsid, (N) and **c,** membrane (M) protein, monomer (m) and insoluble aggregate (a) in hiPSC-CMs, 48 hours post-infection. Scale bar, 50  $\mu\text{m}$ .

**Ext. Data Fig. 5 | Grouping of cardiomyotube nuclei as rosettes or physiological rows. a,**

Phase contrast image of SARS-CoV-2 hiPSC-cardiomyotubes demonstrating nuclear rosette (red broken circle) versus linear row (yellow broken circle) configurations. White arrow designates interposed non-cardiomyocytes excluded from cardiomyotubes. Scale bar, 40  $\mu\text{m}$ . **b,** IHC of cardiomyotube (black broken circle) in BrdU-labeled neonatal pig myocardium demonstrating physiological linear row configuration and equivalent incorporation of BrdU, confirming S-phase cell cycle synchrony of all nuclei, unlike (Fig. 2d). Scale bar, 50  $\mu\text{m}$ .

**Ext. Data Fig. 6 | SARS CoV-2 S-protein tagged with mEmerald at the cytoplasmic tail is expressed, correctly processed, and retains cell-cell fusion function. a,**

Left panel: schematic of SARS-CoV-2 S tagged with mEmerald (mEm) at the cytoplasmic tail. Cleavage at the S1/S2 furin site primes the spike protein for activation. S1, S1 subunit; S2, S2 subunit; N-/C-RBD, N-/C-terminal receptor binding domains and TM, trans-membrane segment. The fusion peptide is shown in blue and heptad repeat 1 and 2 in pink and dark pink, respectively. The monoclonal antibody 1A9, which was used to detect the spike proteins, binds to an exposed loop (purple) located close to heptad repeat 2. Right panel: immunoblot of the CoV-2 S and CoV-2 S-mEm proteins detecting their S0 and S2 subunits. **b,** Super resolution confocal microscopy of CoV-2 S-mEm localization to Vero cell filopodia. Scale bar, 5  $\mu\text{m}$ . **c,** Left panel: cellular localization of the tagged spike protein in HeLa cells transfected with the expression plasmid for S-mEm. This protein was detected either by fluorescence emission (horizontal axis) or by using spike-specific-mAb 1A9 and AF647 conjugated secondary-antibody (vertical axis). Right panel: Schematic of the method used to determine the localization of the spike

protein in non-permeabilized HeLa cells. **d**, Still image from live cell confocal microscopy of recombinant CoV-2 S-mEm transfected in Vero cells. Scale bar, 50  $\mu$ m.

**Ext. Data Fig. 7 | Aberrant electrophysiology in SARS-CoV-2 S generated cardiomyotubes.** **a**, Action potential traces (**a**) and duration at 50% (**b**, APD50) and 90% (**c**, APD90) repolarization comparing control hiPSC-CMs (black) and CoV-2 S-mEm transfected hiPSC-CMTs (red) paced at 1 Hz. **d**, Patch clamp traces of pathological spontaneous beating in CoV-2 S-mEm transfected hiPSC-CMTs. Black arrows indicate delayed after depolarizations (DADs).

**Ext. Data Fig. 8 | a, Characterization of SARS-CoV-2 spike generated electrical dysfunction and its correction by a furin inhibitor.** Still frame images of Fluo-4 AM  $\text{Ca}^{2+}$  imaging in CoV-2 S hiPSC-CMT depicting  $\text{Ca}^{2+}$  tsunami from initiation to termination. Broken circles (yellow, white and red) depict motion of  $\text{Ca}^{2+}$  tsunami peak intensity pulse wave. **b**, Comparison of % area of 40X microscopic field occupied by Fluo-4 AM  $\text{Ca}^{2+}$  tsunami wave pulse signal in control hiPSC-CMs (black) and CoV-2 S hiPSC-CMTs with representative tracings. **c**, Comparison of % area of 40X microscopic field occupied by Fluo-4 AM  $\text{Ca}^{2+}$  sparks in control hiPSC-CMs (black) and CoV-2 S hiPSC-CMTs with representative tracing highlighting sparks in CoV-2 S hiPSC-CMTs. Black arrows indicate  $\text{Ca}^{2+}$  spark examples. **d**,  $\text{Ca}^{2+}$  sparks (% area of 40X microscopic field) in CoV-2 S transfected hiPSC-CMTs inhibited by Decanoyl-RVKR-CMK (20  $\mu$ M) at 24-48 hours. **e**, SARS-CoV-2 S processing (S0 cleavage into S1 and S2) in Vero cells treated with increasing concentrations of Furin inhibitor I (Decanoyl-RVKR-CMK; 0  $\mu$ M, 5  $\mu$ M, 10  $\mu$ M and 20  $\mu$ M) and corresponding phase contrast image of Vero cells transfected with CoV-2 S without (left) and with 20  $\mu$ M Dec-RVKR-CMK at the 72 hour time point.

**Ext. Data Fig. 9 | Aberrant electrophysiology in MERS S generated cardiomyotubes.** **a**, Immunoblot of recombinant MERS spike glycoprotein transfected hiPSC-CM showing spike glycoprotein processing detected by FLAG epitope fused to the C-terminus (only S0 and S2 detected). High molecular weight (>250 kDa) oligomers, presumably trimers, are shown as well. **b**, Anti-FLAG IF microscopy of MERS spike glycoprotein generated hiPSC-CMTs, largest example circled in broken yellow. Scale bar, 50  $\mu$ m. **c**, Confocal microscopy of an EdU pulse-labeled, recombinant MERS spike glycoprotein transfected hiPSC-CMT, analogous to CoV-2 in (Fig. 3d). Scale bar, 20  $\mu$ m. **d**, Bright field microscopy of crystal violet stained recombinant MERS spike glycoprotein transfected hiPSC-CMTs at 5 days post-transfection. Measurements of total nuclei count and surface area of the CMT circled in red are shown. Yellow broken circles highlight colonies of proliferating cells disallowed entry into the CMT. Scale bar, 200  $\mu$ m. **e**, Micro Electrode Analysis (MEA) comparing spontaneous electrical field potentials of control hiPSC-CMs (baseline; black) and MERS S-transfected hiPSC-CMTs (broken red circle) at day-5 post transfection demonstrating fusion-associated degradation of electromechanical depolarization and repolarization phase signals.

## Video Legends

**Supplemental Video 1: Intercellular spread of CoV-2 S-mEm spike glycoprotein and fusion in Vero cells.** Time-lapse confocal fluorescence video microscopy of CoV-2 S-mEm spike glycoprotein transfected Vero cells demonstrating cell-cell fusion and spread of S-mEm spike glycoprotein signal from cell-to-cell. Images captured every 40 minutes over a 12 hour time period starting 24 hours after transfection.

**Supplemental Video 2: Intercellular spread of CoV-2 S-mEm spike glycoprotein and fusion-mediated hiPSC-CMT assembly.** Time-lapse confocal fluorescence video microscopy of CoV-2 S-mEm spike glycoprotein transfected hiPSC-CMs demonstrating cell-cell fusion coupled with spread of S-mEm from cell-to-cell. Images captured every 30 minutes over a 12 hour time period starting 24 hours after transfection.

**Supplemental Video 3:  $\text{Ca}^{2+}$  transients in hiPSC-CMs.**  $\text{Ca}^{2+}$  imaging/video microscopy demonstrating intracellular  $\text{Ca}^{2+}$  transients in control hiPSC-CMs, synchronized, electromechanically-coupled, beating cells studied at day-20 of differentiation after loading with  $\text{Ca}^{2+}$  sensitive tracer, Fluo-4 AM, paced at 1Hz.

**Supplemental Video 4: Pathological  $\text{Ca}^{2+}$  transients – tsunamis and sparks – in SARS-CoV-2 S generated hiPSC-CMTs.** When compared to rhythmic  $\text{Ca}^{2+}$  imaging signal observed by Fluo-4 AM in hiPSC-CMs (Supplemental Video 3),  $\text{Ca}^{2+}$  imaging/video microscopy of CoV-2 S spike glycoprotein generated CMTs paced at 1Hz demonstrates pathological “sparks” (high-frequency, unsynchronized, low-intensity  $\text{Ca}^{2+}$  transients) and “tsunamis” (high-intensity, slowly-moving wave-like  $\text{Ca}^{2+}$  transients that trek across the entire CMT, here from south to north). Still frames captured from this particular CoV-2 S hiPSC-CMT video are shown in (Fig. 5f and Extended Data Fig. 8a).

**Supplemental Video 5: Pathological  $\text{Ca}^{2+}$  sparks superimposed upon normal transients in CoV-2 S generated hiPSC-CMTs.** Fluo-4 AM  $\text{Ca}^{2+}$  imaging/video microscopy of CoV-2 S spike glycoprotein generated CMTs paced at 1Hz demonstrating preserved normal rhythmic  $\text{Ca}^{2+}$  transients as in (Supplemental Video 3) coupled with unsynchronized, low-intensity “sparks” as in (Supplemental Video 4) defining an intermediate stage of phenotypic disorganization before tsunami development.

**Supplemental Video 6: Pathological  $\text{Ca}^{2+}$  tsunamis and sparks in CoV-2 S generated hiPSC-CMTs.** Fluo-4 AM  $\text{Ca}^{2+}$  imaging/video microscopy of CoV-2 S spike glycoprotein generated CMTs paced at 1 Hz demonstrating spurious, low-intensity  $\text{Ca}^{2+}$  sparks and two successive  $\text{Ca}^{2+}$  tsunami-like waves slowly moving from north to south.

## Methods

### Immunofluorescence confocal microscopy of patient myocardium

We obtained patient myocardium in accordance with Michigan Medical Examiner Law for establishing cause, manner and circumstances of death, and in this case for establishing the etiology of fatal myocarditis during a pandemic. Five  $\mu\text{m}$  tissue sections

were generated from formalin-fixed paraffin-embedded tissue blocks. Slides were baked at 60°C for 30 minutes then deparaffinized and rehydrated through sequential incubations in xylenes and ethanol, then rinsed in cold running tap water. Antigen retrieval was done via incubation in 1mM EDTA, pH 8.0 at ~ 95°C for 30 minutes followed by rinsing in dH2O. Sections were blocked for 1 hour in 4% BSA, 0.1% TritonX100 in PBS. Sections were incubated in primary antibody (GeneTex, SARS-CoV-2 Spike mAb 1A9 or Bioss Antibodies, SARS-CoV-2 Nucleocapsid mAb 1C7, plus Proteintech, MYL2 rabbit polyclonal for 1 hour at room temperature. Secondary antibodies (Alexa Fluor 488 or 647 @ 1:1000) were applied for 20 minutes at room temperature. Sections were counterstained with DAPI, mounted under coverslips using Invitrogen Prolong Gold Antifade reagent and imaged using a Zeiss LSM780 or Elyra PS.1 Super Resolution confocal microscope.

### **Spinner culture cardiac differentiation of human-iPSCs**

Obtained under Mayo Clinic IRB protocol, patient and control human fibroblast-derived iPSCs were maintained in mTESR1 basal media with mTESR supplement on plates coated with Geltrex (in DMEM/F12 media). Undifferentiated hiPSCs were transitioned and expanded in suspension/spinner culture in DMEM/F-12 plus Glutamax, StemPro supplement, BSA and bFGF with Rock Inhibitor Y27632 combined with mTESR1 media, and then chemically differentiated by CHIR/IWP-4 into CMs in RPMI 1640 plus B27 minus insulin supplement as beating aggregates. Detailed spinner culture cardiac differentiation protocol is available from J.W.S. upon request. Differentiated hiPSC-CMs were maintained in Gibco™ Cardiomyocyte Maintenance Medium and attached to fibronectin-coated glass coverslips. Human H9 embryonic stem cells (WiCell) were chemically differentiated into CMs using an analogous protocol in monolayer culture. EdU (5-ethynyl-2'-deoxyuridine) labeling of growing iPSC-CMs and detection were done as described by the manufacturer (Thermo-Fisher).

### **SARS-CoV-2 infection of iPSC-CM cells and plaque assays**

SARS-CoV-2/UW-001/Human/2020/Wisconsin (UW-001) isolated from a mild case in February 2020 was used to infect iPSC-CMs in monolayer at multiplicity of infection (MOI) of 1.0 to 0.001 for 30 minutes at 37°C. Unbound virus was then washed-off and fresh media replaced. At the various time points, cells were fixed or extracted and samples were collected, and the vessels decontaminated. An MOI of 0.01 for 24-48 hours proved optimal for observing early stages of SARS-CoV-2 infection in hiPSC-CMs. Beyond 72 hours, even at low starting MOI, cytopathic lysis overwhelmed hiPSC-CM cultures. Highly permissive SARS-CoV-2 infection was observed in 3 different, equivalently differentiated hiPSC-CMs from unrelated donors. Human iPSC-CM produced SARS-CoV-2 was evaluated by plaque-forming assay done in confluent Vero E6/TMPRSS2 cells in TC12 plates infected with supernatant (undiluted and 10-fold dilutions from 10<sup>-1</sup> to 10<sup>-5</sup>) for 30 minutes at 37°C. After initial exposure, the Vero/TMPRSS2 cells were washed three times to remove unbound virus and the media was replaced with 1.0% methylcellulose-media. After an incubation of three days at 37°C, the cells were fixed and stained with crystal violet solution and plaque number counted to determine plaque-forming units (PFU)/ml.

## **Immunocytochemistry**

Coverslips were fixed with neutral buffered formalin for 15 min at room temperature, washed with PBS/0.05% Tween-20 and blocked in (PBS/5% normal goat serum or 3% BSA/0.3% Triton X-100) at room temperature for 1 hour. Coverslips were incubated in primary antibodies diluted in (PBS/1%BSA/0.3% Triton X-100) overnight at 4°C, washed extensively and incubated with diluted secondary antibodies (1:400) at room temperature for 1 hour, then DAPI stained for 10 min at room temperature. Coverslips were mounted on slides with Prolong Gold Antifade Mountant (ThermoFisher) and stored at 4°C. Coverslips were imaged using a Zeiss LSM780 or Elyra PS.1 Super Resolution confocal microscope. Antibodies and reagents for immunocytochemistry included: ACTC1 (Actin  $\alpha$ -sarcomeric mouse mAb clone 5C5 (Sigma), Phalloidin Alexa Fluor-568 conjugated (Invitrogen), SARS-CoV-2 Spike mAb clone 1A9 (GeneTex), SARS-CoV-2 M rabbit polyclonal Ab (Argio Biolaboratories), SARS-CoV-2 Nucleocapsid clone 1C7 (Bioss Antibodies), ACE2 goat polyclonal Ab (R&D Systems) and ATP2A2/SERCA2 rabbit polyclonal Ab (Cell Signaling).

## **Transmission Electron Microscopy**

Cells were washed with PBS and placed in Trump's universal EM fixative<sup>35</sup> (4% formaldehyde, 1% glutaraldehyde in 0.1 M phosphate buffer, pH 7.2) for 1 hr or longer at 4° C. After 2 rinses in 0.1 M sodium phosphate buffer (pH 7.2), samples were placed in 1% osmium tetroxide in the same buffer for 1 hr at room temperature. Samples were rinsed 2 times in distilled water and dehydrated in an ethanolic series culminating in two changes of 100% acetone. Tissues were then placed in a mixture of Epon/Araldite epoxy resin and acetone (1:1) for 30 min, followed by 2 hrs in 100% resin with 2 changes. Finally, samples were placed in fresh 100% resin polymerized at 65° C for 12 hrs or longer. Ultrathin (70-90 nm) sections were cut with a diamond knife and stained with lead citrate. Images were captured with a Gatan digital camera on a JEOL 1400 plus transmission electron microscope operated at 80KeV.

## **Scanning Electron Microscopy**

Fixed in Trump's (1% glutaraldehyde and 4% formaldehyde in 0.1 M phosphate buffer, pH 7.2), tissue was then rinsed for 30 min in 2 changes of 0.1 M phosphate buffer, pH 7.2. Following dehydration in progressive concentrations of ethanol to 100% the samples were critical-point dried. Specimens were then mounted on aluminum stubs and sputter coated with gold/palladium. Images were captured on a Hitachi S4700 scanning electron microscope operating at 3kV.

## **HeLa and Vero cells**

HeLa cells were cultured in Dulbecco's modified Eagle's medium (DMEM) supplemented with 10% FBS. Vero-hSLAM (Vero cells stably expressing human signaling lymphocyte activation molecules, kindly provided by Y. Yanagi; these cells are described simply as Vero cells in this manuscript)<sup>36</sup> were maintained in DMEM supplemented with 10% FBS and 0.5 mg of G418/ml. All cell lines were incubated at 37°C with 5% CO<sub>2</sub>.



## Plasmids

The codon-optimized SARS-CoV2 S-protein gene (YP\_009724390) was synthesized by Genewiz in a pUC57-Amp plasmid (kindly provided by M. Barry). The S-protein coding sequence was cloned into a pCG mammalian expression plasmid<sup>37</sup> using unique restriction sites *Bam*HI and *Spe*I. The SARS CoV S-protein (VG40150-G-N) and the MERS S-protein (C-terminal FLAG tag, VG40069-CF) purchased from Sino Biological, were cloned into the pCG vector for comparative studies. The SARS-CoV-2 S-mEmerald construct was made by cloning the mEmerald sequence (Addgene, Plasmid #53976) to the C-terminal end of the SARS CoV-2 S-protein in the pCG expression vector. A flexible 6 amino acid-linker (TSGTGG) was used to separate the two proteins. All expression constructs were verified by sequencing the entire coding region.

## Immunoblots

Vero cells were transfected with spike protein expression constructs using the GeneJuice transfection reagent (Novagen). The indicated S-protein expression constructs (1 µg) were transfected into  $2.5 \times 10^5$  Vero cells in 12-well plates. Thirty-six hours post-transfection, extracts were prepared using cell lysis buffer (Cell Signaling Technology, #9803) supplemented with cOmplete protease inhibitor cocktail (Roche, Basel, Switzerland) and the proteins separated by sodium dodecyl sulfate-polyacrylamide gel electrophoresis (SDS-PAGE) (4 to 15% gradient) under reducing conditions. The S-proteins were visualized on an immunoblot using the anti-S specific monoclonal antibody 1A9 (GeneTex, GTX632604; 1:2000 dilution) which binds the S2 subunit of SARS CoV and SARS-CoV-2 S-proteins. An anti-mouse horseradish peroxidase (HRP)-conjugated secondary antibody was used to reveal the bands. MERS S-protein was detected using a monoclonal anti-FLAG M2-HRP conjugated antibody (SIGMA, A8592 @ 1:2000) which bound to a C-terminal FLAG-tag. The expression of the mEmerald tag was verified using a polyclonal anti-GFP antibody (Abcam, ab290 @ 1:5000). For hiPSC-CMs infected with SARS-CoV-2 (MOI 0.01, 48 hours), extracts were prepared in CLB as above (but also including PMSF), separated by SDS-PAGE and blotted with S, M and N antibodies as described under Immunohistochemistry above.

## Cell-cell fusion assays

For spike glycoprotein-mediated cell-to-cell fusion,  $1.5 \times 10^5$  Vero cells in 24-well plates were transfected with 0.5 µg of the indicated S-protein expression vector using the GeneJuice transfection reagent (Novagen) and syncytia formation monitored for 24-48 hours post-transfection. Images were collected by Nikon Eclipse TE300 using NIS-Elements F 3.0 software (Nikon Instruments, Melville, NY, USA). For recombinant spike glycoprotein-mediated fusion in hiPSC-CMs, subconfluent day-20 differentiated cells plated on fibronectin-coated glass coverslips in 6-well plates were transfected with 1-2 µg plasmid using Lipofectamine 3000. For CoV-2 S-mEm in hiPSC-CM experiments syncytia formation became obvious within 6 hours of transfection.

## **Furin inhibitor treatment**

Furin Inhibitor I (Decanoyl-RVKK-CMK, Calbiochem, #344930) dissolved in DMSO was added to Vero or hiPSC-CM cell culture medium 2-hours post transfection. Cell-cell fusion was followed for 72-hours (for Vero cells) and 5 days for iPSC-CMS with refreshment of media and inhibitor on day-3. Whole cell extracts were separated on SDS-PAGE and immunoblotted for SARS-CoV-2 S as described above or cells fixed and stained by crystal violet.

## **FACS**

To determine S-protein cell surface expression levels, HeLa cells ( $8 \times 10^5$  in a 6-well plate) were transfected with the indicated S-protein expression plasmids (2  $\mu$ g using GeneJuice transfection reagent). Thirty-six hours post-transfection, cells were washed in PBS and detached by incubating with Versene (Life Technologies) at 37°C for 10 min. The resuspended cells were washed twice with cold fluorescence-activated cell sorter (FACS) wash buffer (phosphate buffered saline, 2% FBS, 0.1% sodium azide) and then incubated with the anti-S-protein mAb 1A9 (GeneTex; 1:50 dilution) for 1 hour on ice. Cells were washed three times with cold FACS wash buffer and incubated with an AF647-conjugated secondary antibody (Thermo Fisher Scientific, a21235 @ 1:200) for 1 hour on ice. After three washes with FACS wash buffer, cells were fixed in 4% paraformaldehyde and analyzed with a FACSCalibur (BD Biosciences, San Jose, CA) cytometer and FlowJo software (Tree Star Inc., Ashland, OR).

## **Calcium imaging**

Untransfected and SARS-CoV-2 S transfected hiPSC-CMs cultured on fibronectin-coated 35mm glass-bottom dishes (MatTek Corporation, Ashland, MA) at 37°C, 5% CO<sub>2</sub> were loaded with 5 $\mu$ M of Fluo-4 AM (Thermo Fisher Scientific, Waltham, MA) with 0.02% F-127 (Thermo Fisher Scientific, Waltham, MA) in Tyrode's Solution (Alfa Aesar, Tewksbury, MA) for 30 minutes. Following wash-out, Tyrode's solution was added and cells were imaged. During imaging, cells were kept in a heated 37°C stage-top environment chamber supplied with 5% CO<sub>2</sub>. Imaging of Ca<sup>2+</sup> transients was taken under a 40X objective using a Nikon Eclipse Ti (Melville, NY) light microscope. Human iPSC-CMs were paced at 1 Hz using an IonOptix MyoPacer Field Stimulator (Westwood, MA). Time-lapse videos were taken at a speed of 20ms per frame for 20s. Each video recording was analyzed for the percent area exhibiting pacing, calcium sparks, and calcium tsunami. The raw data was exported to Excel software (Microsoft, Redmond, WA) and analyzed with a custom Excel-based program in order to normalize for photo bleaching and movement. All values are reported as mean  $\pm$  SEM. Statistical analysis was performed using GraphPad Prism 8 software (San Diego, CA). T-test was used to determine statistical significance between two groups, and a one-way ANOVA followed by Tukey's multiple comparisons test was used to determine statistical significance between 3 groups. A  $P < 0.05$  was considered to be significant.

## **Electrophysiology**

Action potentials (APs) from untransfected or SARS-CoV-2 S-mEmerald transfected hiPSC-CMs were recorded at RT (22-24°C) using current clamp mode at a constant rate of 1 Hz through 5 ms depolarizing current injections of 300-500 pA and gap free configuration with an Axopatch 200B amplifier, Digidata 1440A and pClamp version 10.4 software. The extracellular (bath) solution contained (mmol/L): 150 NaCl, 5.4 KCl, 1.8 CaCl<sub>2</sub>, 1 MgCl<sub>2</sub>, 1 Na-Pyruvate and 15 HEPES, pH adjusted to 7.4 with NaOH. The pipette solution contained (mmol/L): 150 KCl, 5 NaCl, 2 CaCl<sub>2</sub>, 5 EGTA, 5 MgATP and 10 HEPES, pH adjusted to 7.2 with KOH<sup>38</sup>. Data were analyzed using Clampfit and Excel (Microsoft, Redmond, WA), and graphed with GraphPad Prism 8.3 (GraphPad Software, San Diego, CA). All data points are shown as the mean value and bars represent the standard error of the mean. A Student's t-test was performed to determine statistical significance between two groups. A  $P < 0.05$  was considered to be significant.

## **Microelectrode Array (MEA) Electrophysiology**

Human iPSC-CMs plated on fibronectin-coated 24-well Plate with PEDOT Electrodes on Glass (24W300/30G-288; Multichannel Systems, MCS GmbH, Reutlingen, Germany) (12 30-mm diameter micro-electrodes spaced 300 mm apart per well) were cultured as described above. Spontaneous CM electromechanical activity at 37 °C was recorded for 3 minutes following 5 minutes of acclimatization every day after plating before and after transfection with MERS S-FLAG, which was associated with minimal cytotoxicity at low DNA concentration (determined by serial dilution of plasmid DNA). Multinucleated giant cell assembly by cell fusion was followed by phase contrast microscopy and correlated with aberrant field potentials recorded and analyzed by Multichannel Systems software.

## **Time lapse confocal microscopy**

Vero cells were sparsely plated on a glass-bottom 35-mm dish and transfected with 1 µg of the SARS-CoV-2 S-mEmerald expression construct using GeneJuice transfection reagent. Time lapse confocal microscopy with images taken every 30-40 minutes for 12-hours, was performed 24-hours post-transfection on a Zeiss LSM780 equipped with a heated CO<sub>2</sub> chamber. For time-lapse confocal fluorescence video microscopy of CoV-2 S-mEm spike glycoprotein transfected hiPSC-CMs, images were captured every 30 minutes over a 12 hour time period starting 24 hours after transfection on a Zeiss LSM780 equipped with a heated CO<sub>2</sub> chamber.

## **Acknowledgements**

We thank Jeff Salisbury and the Mayo Clinic Microscopy and Cell Analysis Core facility for experimental and technical support and Mike Barry for the SARS-CoV-2 spike coding sequence and the Mayo Clinic Graduate School of Biomedical Sciences for graduate student support (D.R.P. and D.J.C.).

Wanek Family Program for HLHS-Stem Cell Pipeline: Timothy J. Nelson (Director), Boyd Rasmussen and Frank J. Secreto.

776

777

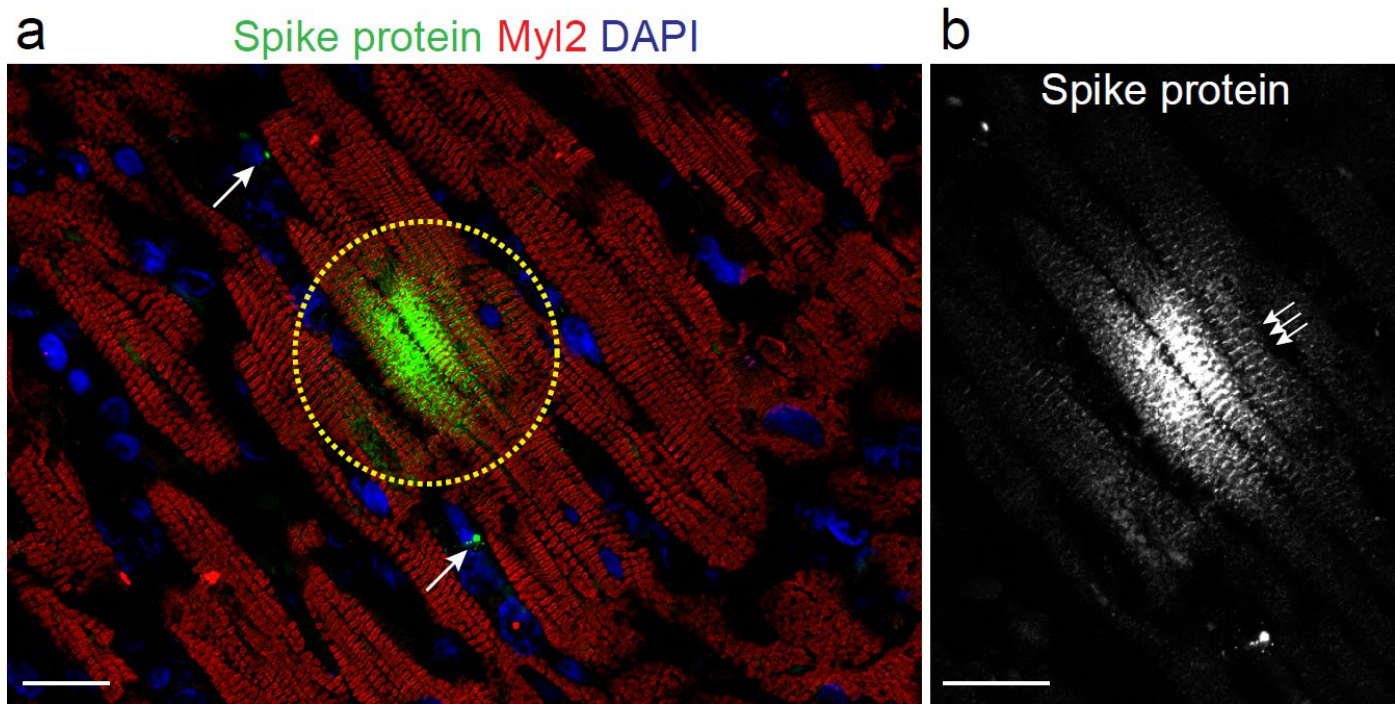


Figure 1



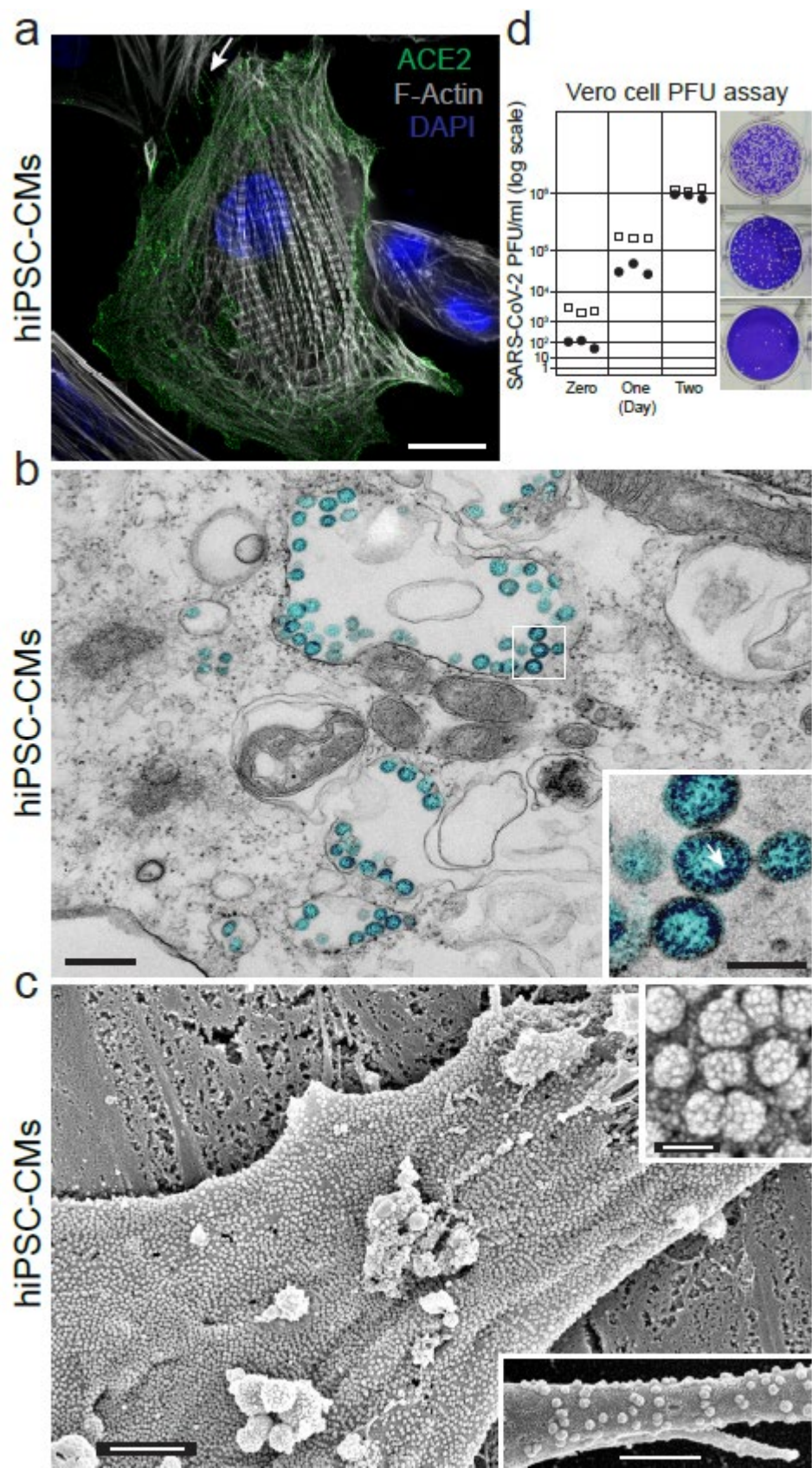


Figure 2



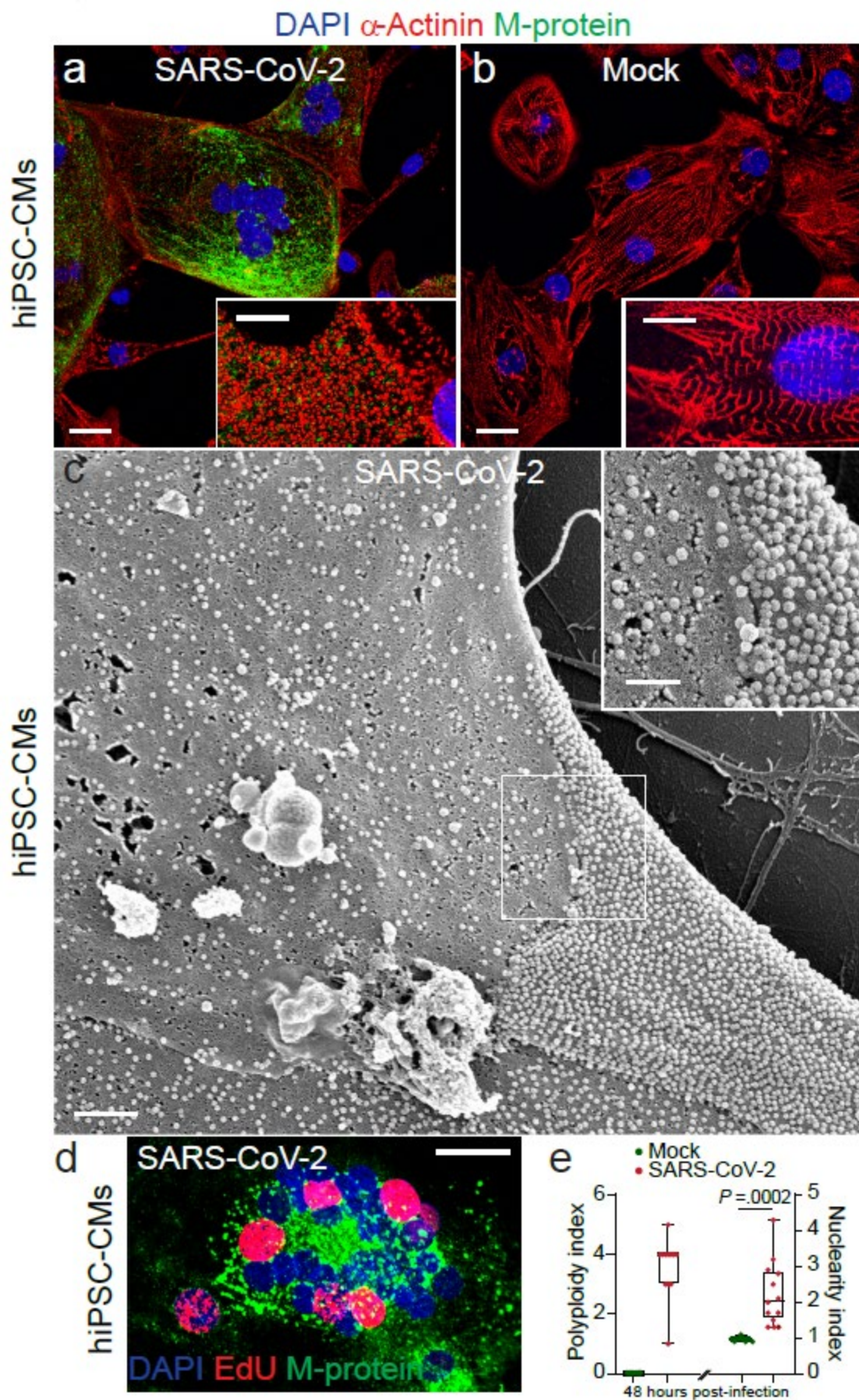


Figure 3

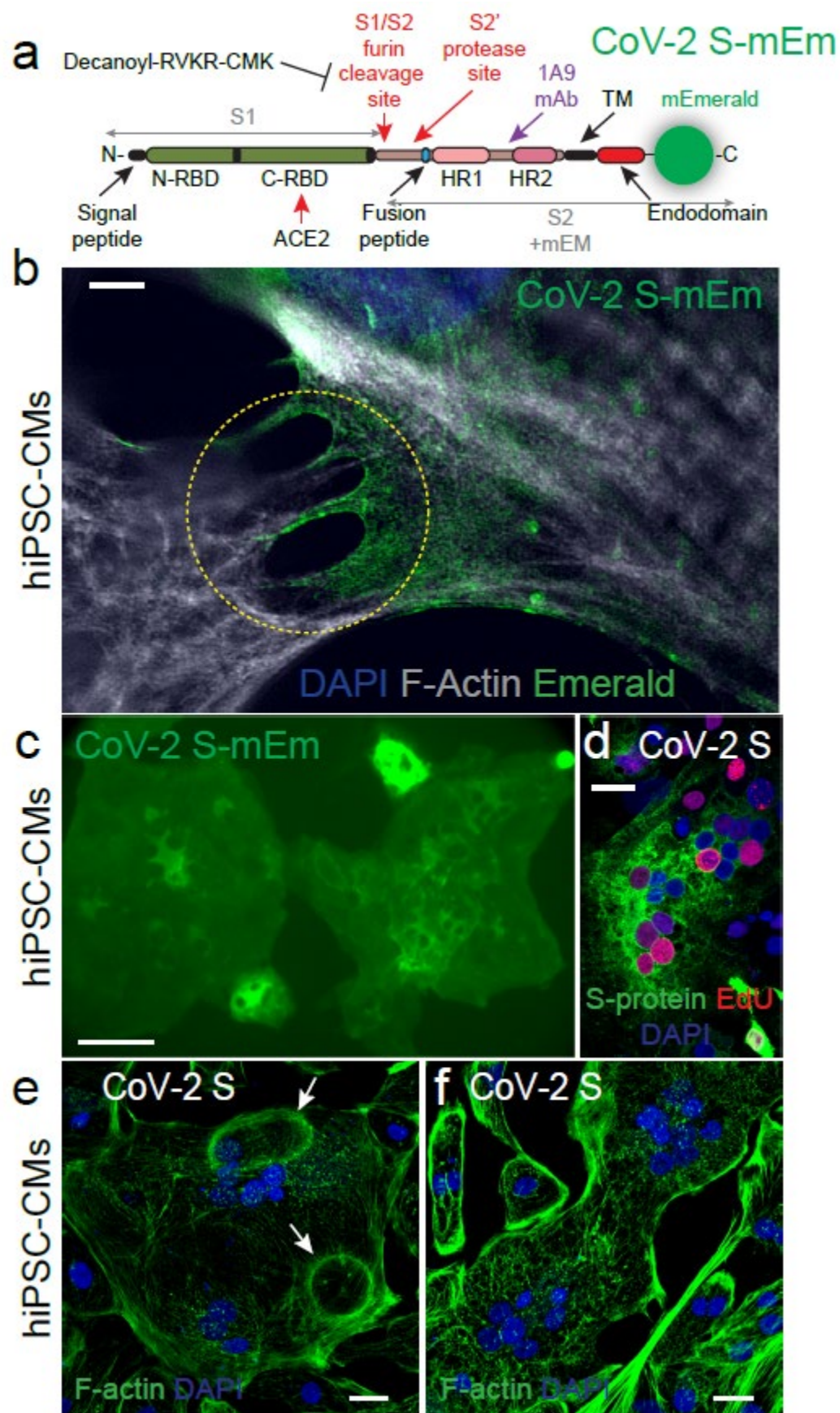


Figure 4



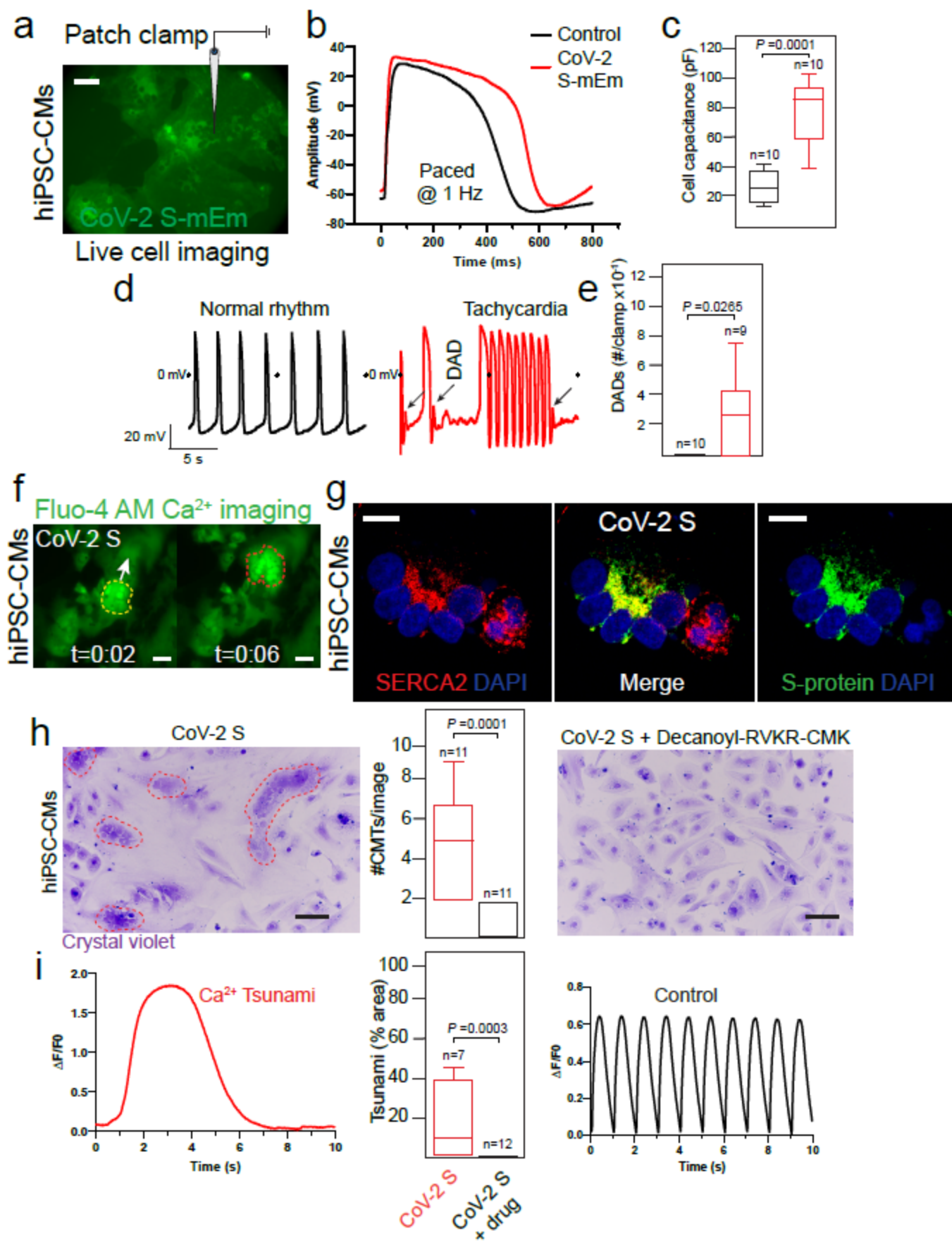


Figure 5